Check for updates

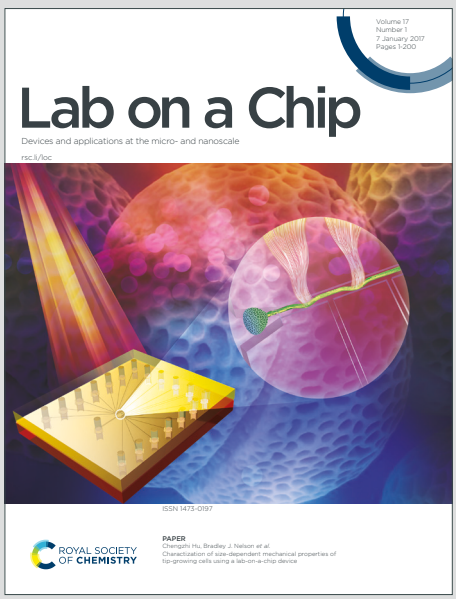
View Article Online
View Journal

Lab on a Chip

Devices and applications at the micro- and nanoscale

Accepted Manuscript

This article can be cited before page numbers have been issued, to do this please use: J. Hwang, S. Yu, C. M. Ross and I. Battiato, *Lab Chip*, 2025, DOI: 10.1039/D5LC00557D.



This is an Accepted Manuscript, which has been through the Royal Society of Chemistry peer review process and has been accepted for publication.

Accepted Manuscripts are published online shortly after acceptance, before technical editing, formatting and proof reading. Using this free service, authors can make their results available to the community, in citable form, before we publish the edited article. We will replace this Accepted Manuscript with the edited and formatted Advance Article as soon as it is available.

You can find more information about Accepted Manuscripts in the Information for Authors.

Please note that technical editing may introduce minor changes to the text and/or graphics, which may alter content. The journal's standard Terms & Conditions and the Ethical guidelines still apply. In no event shall the Royal Society of Chemistry be held responsible for any errors or omissions in this Accepted Manuscript or any consequences arising from the use of any information it contains.

ROYAL SOCIETY OF CHEMISTRY

rsc.li/loc

View Article Online
DOI: 10.1039/D5LC00557D

Journal Name

ARTICLE TYPE

Cite this: DOI: 00.0000/xxxxxxxxxx

Integrated Physics-Based Modeling and Microfluidics for Quantifying Multiphase Carbonate Dissolution in Rocks

Junyoung Hwang,[a‡] Siqin Yu,[a‡] Cynthia M. Ross,[a] and Ilenia Battiato*[a]

Received Date
Accepted Date

DOI: 00.0000/xxxxxxxxxx

Acid dissolution of carbonate formations is critical to the energy transition and relevant to many engineering applications. The dynamics of the dissolution reaction are complex, strongly depend both on the flow properties and sample mineralogy and are further complicated by the production of carbon dioxide gas bubbles from the reactive surface, which renders the system multiphase. Quantifying the impact of multiphase flow conditions on effective reaction rates of carbonate dissolution has challenged experimental methods focused on core-based characterization techniques. In this work, we use microfluidic devices that contain carbonate-rich (86 wt%) rock samples with a cylindrical shape to observe their dissolution upon injection of hydrochloric (HCl) acid under both single and multiphase conditions. The dissolution reaction is visualized and recorded at high temporal resolution using a high-speed camera and is quantified through machine learning (ML)-based image segmentation. First, we combine ML-enabled image analysis with physics-based modeling to estimate the instantaneous reaction rates of carbonate dissolution under single-phase conditions and validate that it follows a first-order reaction rate law. Then, we use the proposed approach to determine the effective dissolution rate under multiphase flow conditions, i.e. when - at higher HCl concentration - the formation of CO_2 bubbles shields the adjacent carbonate surface hindering reaction progress. We find that, under such conditions, the effective reaction rate decreases by one order of magnitude, strongly deviating from the reaction rate law previously determined for single-phase conditions and that current models are not able to capture the impact of gas shielding effects on effective reaction rates under multiphase flow conditions. We also find that the natural chemical heterogeneity of rocks leads to the in situ formation of an unreacted mineral porous layer which serves as the substrate for gas bubbles to nucleate and grow, which changes the conceptual model established for calcite systems.

Introduction

Carbonate dissolution is at the heart of many processes critical to sustainability and the energy transition [1–4], including acidification of carbonate formations during underground gas storage [5–7], caprock destabilization at CO_2 sequestration sites [8], preservation of buildings constructed from carbonate rocks [9,10] and mobilization of heavy metal elements in groundwater [11,12]. Carbonate dissolution in geologic systems often consists of coupled multiphase flow, mass transport and geochemical reactions. Gaseous products formed during acidification reactions can give rise to multiphase flow conditions and have significant impact on the overall reaction progress due both to shielding effects of the reactive solid surface [13] and significant alteration of local velocity [14] and concentration fields [15]. In turn, advective and diffusive transport mechanisms can impact the effective reaction rate to a large extent as they control reactant fluxes to the solid surface and hence, its topological alteration as dissolution reactions progress. Although there is ample evidence that the interplay between multiphase flow, mass transport and reactions dominate the microscale (pore) and macroscale (Darcy) evolution of these systems [16?,17], the strong coupling between these processes as well as their inherent multiscale nature have rendered their quantitative understanding an elusive and formidable task, both experimentally and numerically.

One fundamental scientific problem that still remains open is the quantification of the impact of multiphase flow conditions on carbonate dissolution reaction progress in real rocks and the estimation of effective reaction rates, including their potential deviations from single phase conditions.

For fractured systems, current models estimate the decrease of effective reaction rate in multiphase flow conditions by establish-

[a] Department of Energy Science and Engineering, Stanford University, Stanford, USA. E-mail: ibattiat@stanford.edu

‡ These authors contributed equally to this work.

Published on 15 August 2025. Downloaded by Yunnan University on 8/23/2025 5:33:34 PM.

Lab on a Chip Accepted Manuscript

View Article Online
DOI: 10.1039/D5LC00557D

Published on 15 August 2025. Downloaded by Yunnan University on 8/23/2025 5:33:34 PM.

ing a relationship between the effective reaction and gas saturation[18]. The general assumption, however, is that the reactive interfacial area between liquid and solid is fully determined by the wetting behavior[19,20]. This hypothesis does not account for situations in which the gas phase is generated during dissolution reactions and shields the solid reactive surface from further reactions. More importantly, the current models contain multiple parameters that need to be constrained by a robust, low-cost and rapid experimental method.

Extensive efforts have been put into developing methods to observe complex physicochemical processes in porous media. Among these, time-lapsed micro-CT images have been critical in shedding light on reactive processes occurring at the pore-scale[21–25]. Yet, this methodology lacks in temporal resolution, because the images cannot be recorded simultaneously and in situ as the reaction is occurring. Recent advances in the use of microfluidic devices[26], also known as lab-on-chip systems or micromodels, coupled with high-resolution microscopic cameras have overcome such limitations and enhanced our understanding of the transport behavior within geological systems through direct visualization[27–35]. These microfluidic designs allow controlled and reproducible experiments that can directly visualize fluid flow inside complex network of flow channels at the micrometer scale found in subsurface environments[36–39].

The impact of gas shielding during dissolution reactions in granular porous media was experimentally identified on a calcite-embedded microfluidic model, where CO_2 gas bubbles were formed on the solid sample as a result of calcite dissolution[30,32]. A 76% decrease in the average reaction rate for calcite dissolution was observed under the two-phase condition. Song et al.[13] developed biogenically calcite-functionalized micromodels and observed that grain engulfment by a gaseous CO_2 (i) leads to a complete shut down of dissolution reactions, when the reacting solid becomes entrapped within the generated gas phase[13]. Yet, the calcite samples used in such experiments are not representative of the typical chemical heterogeneity observed in natural rocks. The importance of using naturally occurring mineral substrates on realistic pore-scale structures in controlled micromodels was recognized early on by[40,41] with either microchannels being etched into a natural calcite crystal and sealed with a glass slide or by adding clay to pore surfaces to functionalize silicon micromodels.

More recently, pseudo-two dimensional rocks samples have been embedded in microfluidic chips and imaged both at high spatial and temporal resolution to study the impact of carbonate content and its spatial heterogeneity on the dissolution of fractured systems in shales samples[35]. Ling et al.[35] designed a sample-embedded microfluidic device with which they showed varying properties of carbonate dissolution reaction dependent on heterogeneity of mineral distribution and composition with multiple shale samples comprised of a wide range of carbonate content. Their study of dissolution through artificially fractured shales showed dynamical relationships between fracture volume and mineral surface area determined as a function of carbonate content and its distribution. Such microfluidic design is distinguished in that complex mineral heterogeneity as well as surface roughness and pore-scale fracture topology that characterize real geological samples are replicated and visualized at high temporal and spatial resolution. Following Ling et al.[35], Zhou et al.[42] further investigated porosity/specific area correlations under different flow regimes in fractured systems. While the experimental setup and data collection procedure in[35,42] ensures high temporal resolution and the ability to visualize reaction progress in real time, the data processing still relied primarily on manual segmentation of few representative time-stamped images, and consequently limited the extent to which the full dynamics of these complex processes could be modeled/understood/quantified.

In this study, we extend the use of sample-embedded microfluidic design proposed by Ling et al.[35] to observe the dissolution of cylindrical carbonate-rich shale samples due to flow of hydrochloric (HCl) acid solutions at varying concentrations at single and multiphase flow conditions. In a controlled microfluidic chamber where the carbonate-rich samples are relatively uniform in mineral distribution, the acid concentration dictates the reaction rate. Moreover, as the reaction rate (i.e., rate of gas evolution) becomes greater than the rate of gas dissolution into surrounding fluid, the reaction becomes multiphase with the formation of CO_2 bubbles. The evolution and distribution of these bubbles control the progression of subsequent reactions.

We propose a workflow integrating optical imaging of dissolution processes at high spatial and temporal resolution with analytical modeling and ML-based segmentation strategies to, first, estimate and validate single-phase dissolution reaction rates, and subsequently, calculate dissolution reaction rates under multiphase flow conditions. We then verify our optical observation with microscale characterization including scanning electron microscopy (SEM) and energy dispersive X-ray spectroscopy (EDS) imaging. The combination of high temporal and spatial resolution images with ML-enabled image segmentation allows us to quantify the impact of CO_2 bubbles on dissolution and its deviation from the rate law determined under single phase flow. Furthermore, SEM and EDS imaging enable us to observe the mineralogical composition of the reacted surface front after the dissolution reaction has taken place for both single and multiphase reactions. The findings from this study (i) provide the experimental and theoretical basis for the determination of instantaneous reaction rates in multiphase environments, (ii) demonstrate the impact of chemical heterogeneity to build more accurate conceptualizations of natural rock dissolution, and (iii) show that current models accounting for multiphase flow effects on effective reaction rates can significantly underestimate the bubble shielding effect, even before reaction shutoff occurs.

Experimental

Sample Description and Preparation

In this study, we employ six carbonate-rich shale samples, here referred to as Marcellus samples and denoted as MCR1-MCR6. These Marcellus samples contain 86% carbonate (calcite, $CaCO_3$, and dolomite, $CaMg(CO_3)_2$) with other minerals, such as quartz, feldspar, and pyrite, accounting for the remaining mineralogy. The Marcellus samples are ground and polished into a cylinder (2500 μm diameter by 200 μm height) as shown in Figure 1A. The

Lab on a Chip Accepted Manuscript

View Article Online
DOI: 10.1039/D5LC00557D

Published on 15 August 2025. Downloaded by Yunnan University on 8/23/2025 5:33:34 PM.

Lab on a Chip Accepted Manuscript

polishing is achieved by using progressively finer sandpaper from 44 μm to 2.6 μm. The upper and bottom surface of each sample are polished in this manner to enable its subsequent embedding in the microfluidic chip (Figure 1B). After sample preparation, the six samples are considered replicas of each other with the same composition. Although we focus on carbonate-rich shale samples here, the same protocol for sample preparation can be used on other rock types.

Pre- and Post-reaction Characterization and Sample-Embedded Microfluidic Cell

After sample preparation, pre-reaction characterization is performed by SEM and EDS imaging for mineral identification and distribution using JEOL JSM-IT500HR environmental SEM with a Thermo Fisher Scientific EDS system and Pathfinder Pinnacle X-ray microanalysis 2.4 software. Details can be found in Supporting Information.

The design and dimensions of the micromodel features are shown in Figure 1. The polydimethyl-siloxane (PDMS) mold is fabricated by etching the channel and chamber design onto a silicon wafer through reactive ion etching (Plasma-Therm Versaline ICP) with a depth of 200 μm. Other dimensions of the micromodel are shown in Figure 1C. The surface of the etched silicon is then coated with C_4F_8 that acts as an anti-sticking agent between the treated silicon wafer surface and PDMS. The PDMS solution (10:1 weight ratio of elastomer base and curing agent) is poured into the fabricated mold to achieve a complementary pattern after curing. One rock sample is then placed inside the reaction chamber of the PDMS block. The PDMS block is placed on a glass slide coated with a thin layer of PDMS after treating the surfaces with plasma (Plasma Etch PE-50) and heated to $90°C$ for at least $3h$ for bond formation. The PDMS coating on the glass slide is designed to guarantee both that the sample is immobile during flow experiments, and that top and bottom surfaces of the flow chamber have the same wettability. Note that the top and bottom surfaces of the rock sample are isolated from the flow chamber. The fabricated microfluidic device is pseudo-2D, where any top-view area variation can be captured and recorded by the microscope (Ti-E; Nikon Instruments Inc.). After the dissolution experiment, the sample is retrieved from the microfluidic device by cutting the PDMS block over the sample for post-reaction SEM and EDS characterization. The workflow of this entire protocol is summarized in Figure 1D.

Reactive Flow Experiments

In all reactive transport experiments (both single and multiphase), we first saturated the microfluidic cell with deionized water; then the acid is injected with a 25 mL syringe (Hamilton) using a Harvard pump at a flow rate of 1000 $\mu L/h$. The values of the volumetric flow rate correspond with an average velocity $U \sim 2.5 \times 10^{-4}\ m/s$ in the channel. The acid solutions are prepared by diluting 32 wt% of HCl from the same batch. The dissolution experiments are run for at least 5 h. The dissolution of the Marcellus samples via HCl injection is recorded with a high-speed camera (Hamamatsu Flash LT Monochrome) connected to a microscope at a frame rate of 100 ms.

Single-phase dissolution of the Marcellus samples is achieved when the rate of CO_2 dissolution in water is greater than that of CO_2 evolution from the reaction due to low acid concentrations. Soulaine et al.[30] has shown that single-phase dissolution occurs with HCl concentrations below 0.05 wt% when applied to a calcite sample. In this study, HCl concentrations of 0.040, 0.025, and 0.010 wt% are used for single-phase dissolution flow experiments on Samples MCR1, MCR2 and MCR3, respectively. The low acid concentrations prevent CO_2 bubbles from nucleating at the rock surface, and our experimental results confirm this. The experiments using 0.01 and 0.04 wt% HCl are repeated on Samples MCR4 and MCR5 to confirm the experimental repeatability (see Supporting Information). The multiphase experiment is performed with an acid concentration of 0.5 wt% on Sample MCR6.

Image Segmentation

The recorded images are processed using an image segmentation workflow that utilizes the Random Forest algorithm with *ilastik* based on user-annotated images[43]. The segmentation serves the purpose of classifying the heterogeneous image into sample, bubbles and background based on the intensity, edges and texture so that we can extract the sample area along with the time for further analysis. In a single-phase experiment, using less than 1% of the entire image dataset as a training set generates sufficient classifiers that segment the images well from visual inspection. More details regarding image segmentation can be found in the Supporting Information.

Reaction Kinetics and Data Analysis

The following surface reactions occur during dissolution of calcium carbonate ($CaCO_3$) by HCl:

$$CaCO_3(s) + 2HCl(aq) \rightarrow CaCl_2(aq) + CO_2(g) + H_2O(l) \quad (1)$$

$$CO_2(g) \rightarrow CO_2(aq) \quad (2)$$

$$CaCO_3(s) + CO_2(aq) + H_2O(l) \rightarrow Ca(HCO_3)_2(aq) \quad (3)$$

where Equation 2 is the dissolution of CO_2 gas into the surrounding liquid phase represented by the following gas-liquid mass transfer rate equation:

$$m = k_m A_b (C^{sol} - C^{l}) \quad (4)$$

where m [mol s^{-1}] is the rate of mass transfer, k_m [mol $m^{-1}s^{-1}$] is the gas-liquid mass transfer coefficient, A_b [m^2] is the contact area between the bubbles and the surrounding fluid, C^{sol} and C^{l} are solubility of CO_2 and concentration of CO_2 in the surrounding liquid [mol m^{-3}], respectively[44].

The rate of reaction, r_t [mol s^{-1}], shown in Equation 1 can be expressed as:

$$r_t = -\frac{d[CaCO_3]}{dt} = -\frac{1}{2}\frac{d[HCl]}{dt} = \frac{d[CO_2]}{dt} \quad (5)$$

where the rate of $CaCO_3$ or HCl consumption according to their stoichiometric ratios must equal the rate of CO_2 generation.

View Article Online
DOI: 10.1039/D5LC00557D

Published on 15 August 2025. Downloaded by Yunnan University on 8/23/2025 5:33:34 PM.

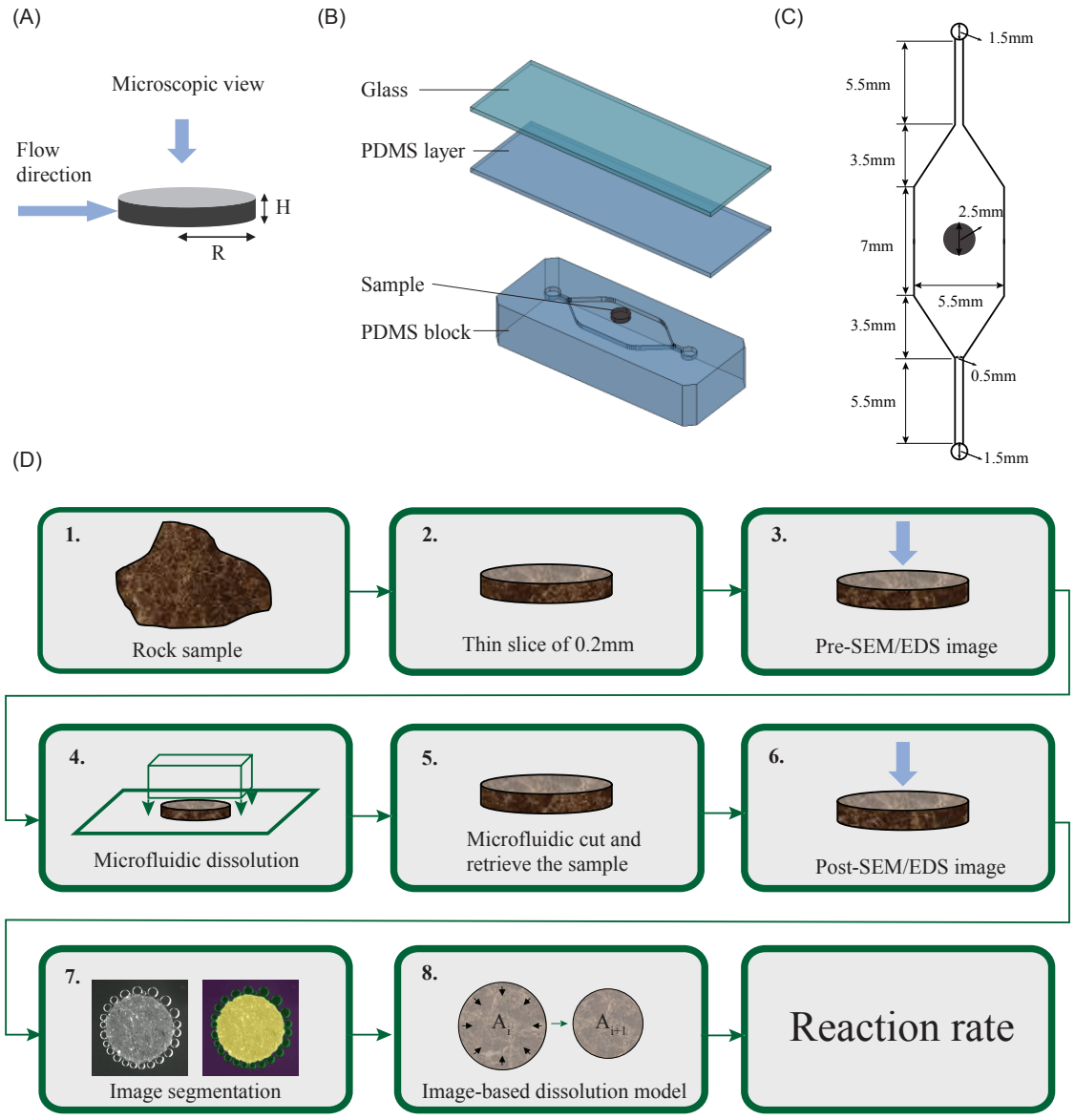


Fig. 1 Graphical representation of (A) polished cylindrical sample (H - 200 μm, R - 1250 μm), (B, C) sample-embedded micromodel and its dimensions, and (D) workflow of dissolution experiment protocol. During reactive flow experiments, the HCl acid solution comes in contact with the side surface of the sample (shown in dark gray) and the top-view of the sample is observed via the microscope (A).

While we are not able to monitor the consumption of HCl or the generation of CO_2, we are able to visualize dissolution of the circular carbonate sample. The rate of surface reaction [mol $m^{-2}s^{-1}$] is defined as the following:

$$r_s = -k[\mathrm{HCl}]^n \tag{6}$$

where the k is the reaction rate constant [m s^{-1}] and n is the reaction order. The rate of absolute reaction [mol s^{-1}] is then defined as:

$$r_t = -kS[\mathrm{HCl}]^n \tag{7}$$

where $S = 2\pi RH$ is the surface area on which reaction occurs shown in dark gray in Figure 1A, under the hypothesis that the

Lab on a Chip Accepted Manuscript

View Article Online
DOI: 10.1039/D5LC00557D

Published on 15 August 2025. Downloaded by Yunnan University on 8/23/2025 5:33:34 PM.

dissolution front is quasi-two-dimensional (2D) (for experimental evidence that the quasi-2D assumption of the sample before and after reaction is valid, see Supplementary Information).

Rewriting S in Equation 7 results in the following:

$$r_t = r_s S = r_s 2(\pi A)^{\frac{1}{2}} H \tag{8}$$

where $A = \pi R^2$ is the area visualized through microscope shown in light gray in Figure 1A. The rate of absolute reaction is alternatively defined as:

$$r_t = -H \frac{dA}{dt} \rho x_c \tag{9}$$

where ρ is the molar density of $CaCO_3$ (27.09 kmol/m^3) and x_c is the $CaCO_3$ content in the sample (0.84). Combining Equations 8 and 9 results in:

$$r_s \; 2(\pi A)^{\frac{1}{2}} H = -H \frac{dA}{dt} \rho x_c. \tag{10}$$

Rearranging Equation 10 yields:

$$r_s = -\frac{dA/dt}{A^{\frac{1}{2}}} \frac{\rho x_c}{2(\pi)^{\frac{1}{2}}} \tag{11}$$

which provides an explicit relationship between the rate of surface reaction and the time-varying area of the sample and its time derivatives, which can be directly collected and/or approximated through the microscope high-temporal resolution optical imaging and image segmentation. The derivative $-dA/dt$ in (11) can be approximated using the recorded images at discrete times t_i and t_{i+1} by means of an explicit forward Euler method as:

$$-\frac{dA/dt}{A^{\frac{1}{2}}} = \left(\frac{A_i - A_{i+1}}{t_{i+1} - t_i}\right) \cdot \left(\frac{A_{i+1} + A_i}{2}\right)^{-\frac{1}{2}}, \tag{12}$$

where $A_i = A(t_i)$ and $A_{i+1} = A(t_{i+1})$. However, due to the noise in the image data originating from the resolution of segmented images at short time intervals (see Supporting Information for details), we employ a differentiation interval, with the derivative dA/dt at t_i approximated as

$$\left(\frac{\partial A}{\partial t}\right)_i = \frac{1}{t_i} \left(\frac{\partial A}{\partial \log t}\right)_i$$

$$= \left[\frac{\log\left(\frac{t_i}{t_k}\right) A_j}{\log\left(\frac{t_j}{t_i}\right) \log\left(\frac{t_j}{t_k}\right)} + \frac{\log\left(\frac{t_j t_k}{t_i^2}\right) A_i}{\log\left(\frac{t_j}{t_i}\right) \log\left(\frac{t_i}{t_k}\right)} - \frac{\log\left(\frac{t_j}{t_i}\right) A_k}{\log\left(\frac{t_i}{t_k}\right) \log\left(\frac{t_j}{t_k}\right)} \right] \tag{13}$$

where t_j and t_k are selected such that

$$\log(t_j) - \log(t_i) > \varepsilon, \quad \log(t_i) - \log(t_k) > \varepsilon, \tag{14}$$

and ε is known as differentiation interval. In an experiment where the rate expressed by Equation 11 is smaller than that expressed by Equation 4, single-phase reaction occurs, where the formation of CO_2 gas bubbles is not observed.

Figure 2 shows the (single-phase) reaction rate calculated for Marcellus sample MCR1 reacted with HCl concentration of 0.04 wt%. While the overall trend of reduction in observed sample area due to dissolution is evident (Figure 2A and B), the high-temporal resolution of the recorded images results in largely scattered data when just the neighboring data points are used in the calculation according to Equation 12 with a significant number of data points in the physically implausible regime of negative reaction rates. Instead, applying Equation 13 reduces the noise in the calculation of the time derivative, and, as such, guarantees that most data points lie in the positive reaction rate regime.

Results and Discussion

Single-phase Reaction rate constant

We first determine the reaction constant and order under single-phase dissolution conditions, i.e. when $C^{\mathrm{l}} < C^{\mathrm{sol}}$, to ensure the image-based estimation is consistent with previously reported data. During single-phase reaction experiments, the dissolution of carbonate is continuous and not hindered by the evolution of CO_2 bubbles as shown in Figure 3A. As discussed in the following section on SEM/EDS images, the dissolution inside the reaction chamber of the microfluidic device occurs uniformly across the reactive surface ensuring the sample remains pseudo-2D. The fact that the left edge has slightly greater dissolution rate than the right edge is attributed to the flow direction being from left to right. The slope and intercept of the following equation (recast from Equation 6) correspond to the reaction order and constant, respectively:

$$\log(r_s) = n \log(c_{\mathrm{HCl}}) + \log(k), \tag{15}$$

where r_s is calculated from (11), after ML-enabled image processing and segmentation. Single-phase flow experiments are conducted at three different HCl inlet concentrations: 0.040%, 0.025% and 0.010%, each denoted as MCR1, MCR2, and MCR3, respectively. The reaction rates are determined to be 1.51×10^{-4} mol m^{-2} s^{-1}, 6.36×10^{-5} mol m^{-2} s^{-1} and 4.48×10^{-5} mol m^{-2} s^{-1}, respectively (solid symbols in Figure 3 B). The experiments with HCl concentrations 0.040% and 0.010% are repeated to confirm the reproducibility of the reactive flow experiments, and they yield reaction rates of 1.64×10^{-4} mol m^{-2} s^{-1} and 4.72×10^{-5} mol m^{-2} s^{-1}, respectively (see Supporting Information for details), within the error bounds of the previously determined values. This shows the repeatability of the experimental methodology.

Figure 3B (dashed line) shows a linear fit of the reaction rates determined in this study and leads to the rate constant and reaction order of 4.8×10^{-3} and 0.81, respectively, that correspond to a rate law close to first-order reaction[45–47]. Specifically,

$$r_s = 4.80 \times 10^{-3} (c_{\mathrm{HCl}})^{0.81}. \tag{16}$$

The rate constant, estimated through the proposed ML-enabled physics-based modeling, compares well with the value obtained by Soulaine et al.[30], where the authors calibrated the reaction rates in the numerical code to ensure a match between the size/shape of the calcite grain observed experimentally and that predicted numerically.

Lab on a Chip Accepted Manuscript

View Article Online
DOI: 10.1039/D5LC00557D

Published on 15 August 2025. Downloaded by Yunnan University on 8/23/2025 5:33:34 PM.

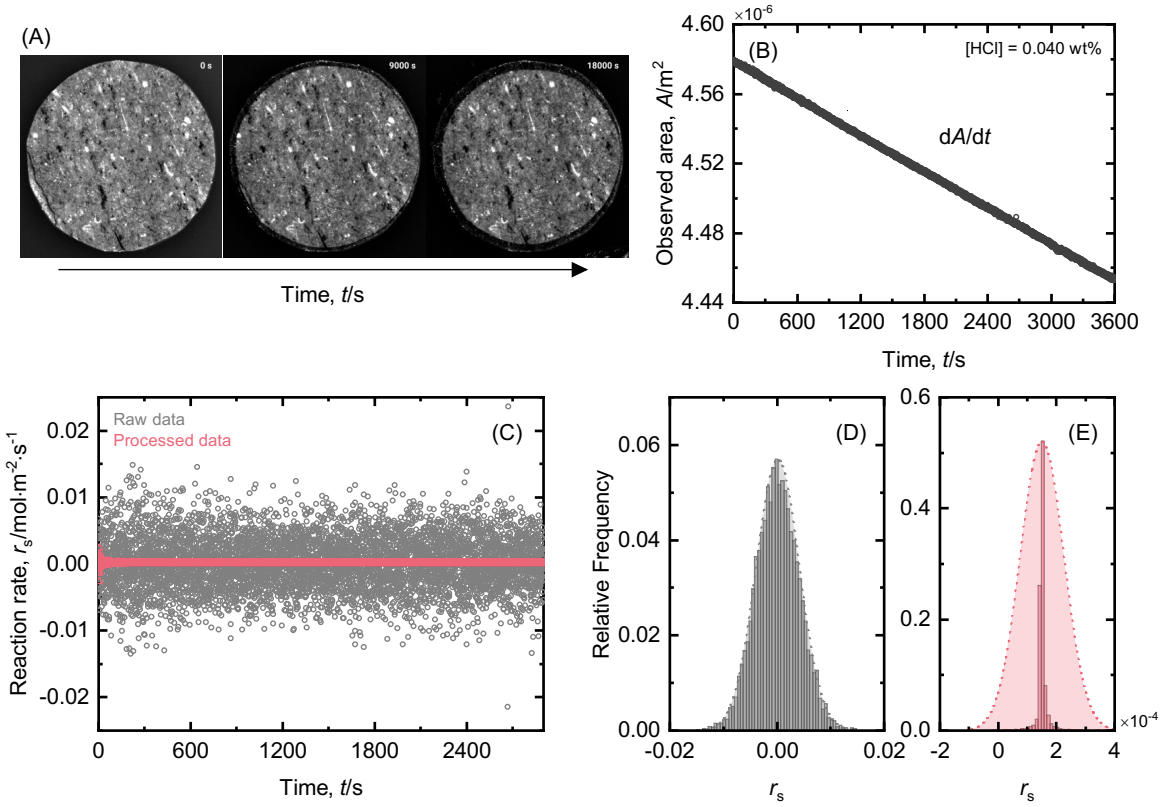


Fig. 2 (A) Recorded images of dissolving Marcellus sample when reacted with HCl solution (0.04%) at three different time points: $0, 9000s, 18000s$; (B) observed sample surface area plotted against time in the last $3600h$ of the reactive flow experiment (total experiment is over $5h$), where the slope represents dA/dt; and (C) reaction rate, r_s, plotted against time using Equation 12 (dark gray) and Equation 13 (light red), distributions of which are shown in (D) and (E), respectively.

Multiphase Reaction Rate Constant

After confirming the robustness of the proposed method to estimate rates of reactions by combining ML-enabled high temporal resolution optical imaging as well as physics-based modeling, we apply the method to estimate reaction rates under multiphase flow conditions, when gas shielding effects cannot be neglected. Figure 3C shows dissolution at HCl concentration of 0.50%. The reaction begins with nucleation with CO_2 gas bubbles at the reacting surface leading to multiphase dissolution, displays a fundamentally different behavior compared with single-phase dissolution (Supporting material movie S2). The CO_2 bubbles grow as more HCl solution is introduced in the reaction chamber, eventually covering most of the surface as shown in Figure 3C. If the bubbles are removed from the surface due to coalescence, new bubbles can rapidly nucleate in situ. This indicates that dissolution selectively occurs between the gas bubbles where reactive surface is exposed to HCl solution. Note that the small droplets contained inside the CO_2 bubbles are due to water condensation on the PDMS, since the latter is permeable to CO_2 [48].

We calculate the reaction rate under multiphase reaction conditions at three different time instances: after bubbles have started nucleating, during bubble growth, and finally when bubbles have nearly completely surrounded the rock sample. The reaction rates directly determined from the dissolution experiments for these three time stamps are 9.29×10^{-4} mol m^{-2} s^{-1}, 2.85×10^{-4} mol m$^{-2}s^{-1}$ and 1.45×10^{-4} mol m^{-2} s^{-1}, respectively. Instead, the reaction rate estimated from the single-phase reaction kinetic relationship, (3), yields 9.59×10^{-4} mol m^{-2} s^{-1}. This shows that the reaction rate directly estimated from images can still agree well with the reaction kinetic relationship when the bubbles just nucleated. However, as dissolution progresses under multiphase conditions, the effective reaction rate decreases significantly as gas saturation increases. When the bubbles have almost completely covered the entire rock surface, the reaction rate can decrease by nearly one order of magnitude as indicated in Figure 3D. Furthermore, differently from the relatively uniform dissolution observed under single phase conditions, at lower pH dissolution occurs selectively at the sample surface exposed between CO_2 bubbles resulting in uneven interfacial receding speed after reaction (SI Figure S4 and S5). Also, particle mobility was observed during multiphase reaction showing stronger mechanical instability with high HCl concentration. Figures 3B and D summarizes the reaction rates of both single- (HCl concentration of $0.040; 0.025; 0.010\%$ and multiphase (0.50%) dissolution reaction of Marcellus samples.

Lab on a Chip Accepted Manuscript

View Article Online
DOI: 10.1039/D5LC00557D

Published on 15 August 2025. Downloaded by Yunnan University on 8/23/2025 5:33:34 PM.

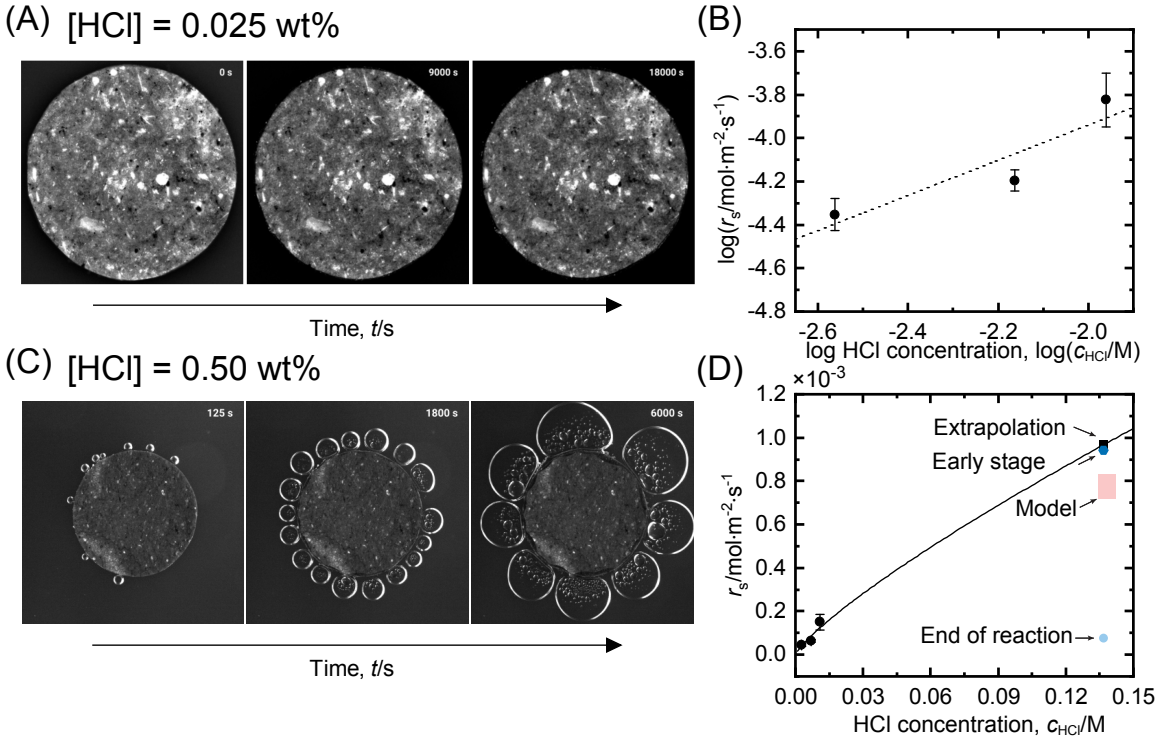


Fig. 3 (A) Recorded images of dissolving Marcellus sample when reacted with relatively high pH HCl solution (0.025%) at three different time instances: 0, $9000s$ and $18000s$; (B) logarithmic plot of reaction rate against HCl concentration; (C) recorded images of dissolving Marcellus sample when reacted with low pH HCl solution (0.50%) at three different time instances: $125s$, $1800s$ and $6000s$; and (D) Comparison between the experimental and calculated dissolution rate at low pH condition.

Impact of secondary minerals

The use of a real rock also highlights the critical importance of chemical heterogeneity on multiphase reactive transport phenomena, which cannot be observed in experiments involving calcite samples. We find that the bubbles generated by the dissolution of carbonates in the rock are *physically separated from the reacting boundary*, i.e. they nucleate and remain pinned on the outer boundary of the unreacted mineral (silicates) instead of the inner dissolution boundary (Figure 4(C)). This is also confirmed by the microscale characterization in Figure 5(C) and (D). Less reactive silicates (marked in green) in Figure 5(D) give rise to a porous layer behind the moving reacting front. This phenomenon is not reported for the calcite sample dissolution because the reactive mineral interface corresponds with the outer solid boundary of the dissolving grain at every instance in time, as conceptualized in Figure 4(A). It is important to emphasize that while the formation of an altered layer has been previously reported[49], to the best of our knowledge, the observation that gas bubbles remain physically separated from the reacting interface, and that their shielding effect is mediated by the altered layer had not been experimentally observed before in similar setups. We expect this phenomenon to become increasingly important at lower carbonate contents where the unreacted minerals would form a distinct porous layer with a porosity smaller than that observed for high carbonate content rocks. We hypothesize that the formation of this porous layer (i) may dominate the transport of reacting species to the reactive interface for decreasing carbonate contents, (ii) may significantly alter the interplay between different physical processes (advection, diffusion, nucleation, bubble growth) compared to experiments on calcite samples and (iii) will likely require the development of reactive models that can account for its thickness, porosity and permeability as a function of mineral composition and also distribution. A conceptualization of this phenomenon is shown in Figure 4(B).

Implications for modeling effective reaction rate at Darcy scale

In reservoir-scale simulators such as ToughREACT, the effective reaction rate decrease can be linked with gas saturation by the following relationship[18,19],

$$r(S_g)/r(S_g = 0) = (1 - S_g)^{1+\gamma}, \tag{17}$$

where γ is known as the active fracture parameter in the range of $[0 - 1]$[18,50]. In our case, we manually label the bubbles area on the image at $t = 9000s$ and find that the gas saturation is 0.19. Therefore, the maximum decrease of effective reaction rate predicted by Equation 17 is $[0.66 - 0.81]$, which is shown as the pink area in Figure 3D. However, a comparison with the effective reaction rate measured directly from the microfluidic experiment through image processing at early (dark blue dot in Figure 3D) and late (light blue dot in Figure 3D) times shows a big discrepancy with the aforementioned model prediction.

Figure 3D shows that the effective reaction rate measured from

Lab on a Chip Accepted Manuscript

View Article Online
DOI: 10.1039/D5LC00557D

Published on 15 August 2025. Downloaded by Yunnan University on 8/23/2025 5:33:34 PM.

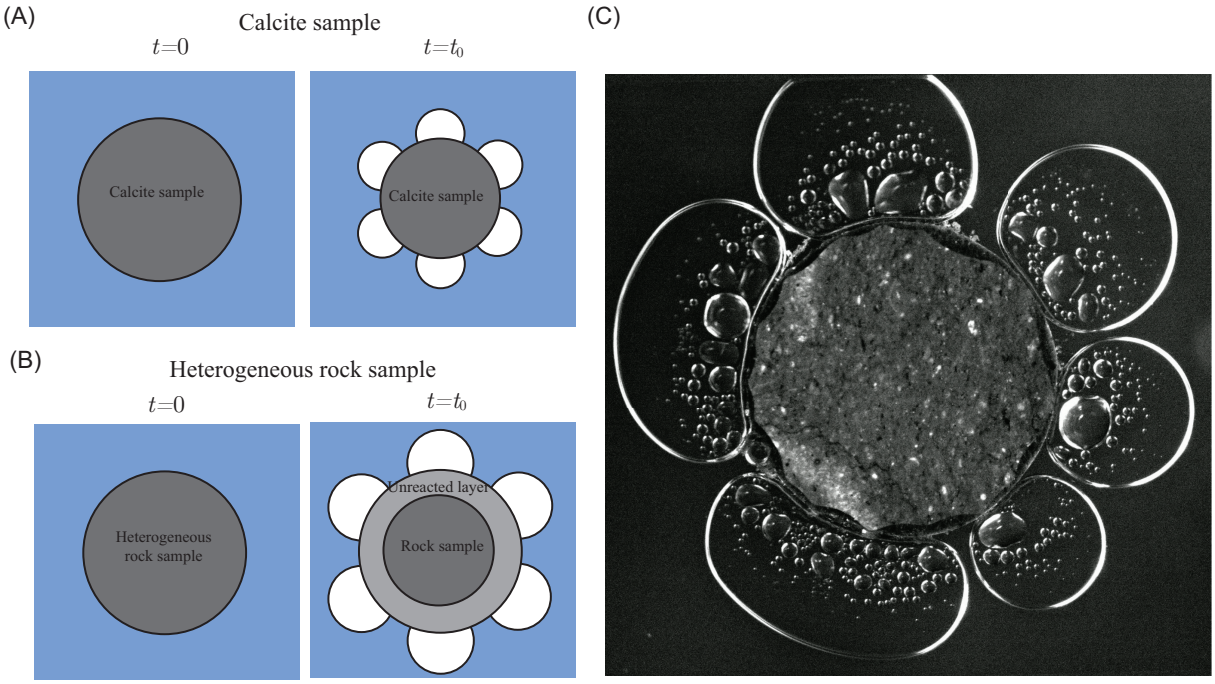


Fig. 4 (A) The conceptual model established by calcite dissolution experiment (B) The conceptual model based on heterogeneous rock dissolution (C) Recorded image of a dissolving heterogeneous rock sample.

experiments is consistent with the reaction kinetic relationship extrapolated to lower pH from the single-phase experiments only at an early stage of the experiment, when the bubbles are small. However, as the reaction progresses, the bubbles start to grow and cover a large portion of the sample surface, significantly slowing down the reaction. At the end of the experiment, i.e. at $t = 9000$ sec, the effective reaction rate has decreased nearly by one order of magnitude due to significant shielding effects. Equation (17) significantly underestimates the bubble shielding effect, because the model only takes wetting behavior into account and neglects that gas bubbles can be generated from the reaction occurring on the solid-liquid interface.

Static Images

Static images of pre- and post-reaction carbonate samples are shown in Figure 5. The EDS images of the post-reaction carbonate samples for single-phase dissolution experiments show that carbonate samples in the microfluidic device react in a pseudo-2D manner (see Supporting Information for details). Also, remnant materials that surround the carbonate sample after reaction, as shown in Figure 2A, are unreacted silicates (SiO_2-bearing) as indicated by its *Si* content. The SEM images of post-reaction carbonate samples of multi-phase dissolution experiments show disrupted surface and recession in the interface only where bubbles do not provide protection from direct contact with acid solution.

Conclusion

Carbonate dissolution is critical to a variety of processes in geologic systems. Because CO_2 is produced during acidification reactions of carbonate-rich rocks, a gas phase can be formed at the interface between the rock and the reacting fluid and dramatically control the subsequent progress of the dissolution reaction. Despite being long recognized, the quantitative impact of multiphase flow conditions on effective reaction rates remains an open question, although their accurate estimate is foundational to the further development of, e.g., porosity-permeability scaling relationships under multiphase flow conditions. We investigated the dynamics of mineral dissolution of carbonate-rich Marcellus shale samples through segmentation of recorded images of carbonate dissolution taking place inside microfluidic reaction chambers. By tightly integrating high spatial and temporal resolution images of shale dissolution experiments in microfluidic chips with ML-enabled segmentation and physics-based modeling, we were able to determine single-phase carbonate dissolution rates at three different HCl concentrations at relatively high pH levels (with two repeat experiments) and validated the findings against previously reported experimental rate data. We then applied the methodology to calculate the effective rates under multi-phase dissolution conditions where CO_2 gas bubbles are generated at higher HCl concentrations, i.e. at lower pH.

The reactive flow experiments below HCl concentration of 0.04% show the sample area reducing continuously without any CO_2 gas phase forming. Due to the lack of a gas phase, the reacting surface of the embedded sample is always exposed to the HCl solution throughout the experiment. The SEM/EDS mosaic indicate that the reaction occurs uniformly at the reacting surface while exposing non-reactive silicate particles as the reaction progresses. The rate law calculated from the reaction rates at three different HCl concentrations under the single-phase environment shows close to first-order reaction with carbonate mineral reactivity to HCl acid linearly increasing with increasing HCl concentration. However, the rate law is no longer applicable to when HCl

Lab on a Chip Accepted Manuscript

View Article Online
DOI: 10.1039/D5LC00557D

Published on 15 August 2025. Downloaded by Yunnan University on 8/23/2025 5:33:34 PM.

Lab on a Chip Accepted Manuscript

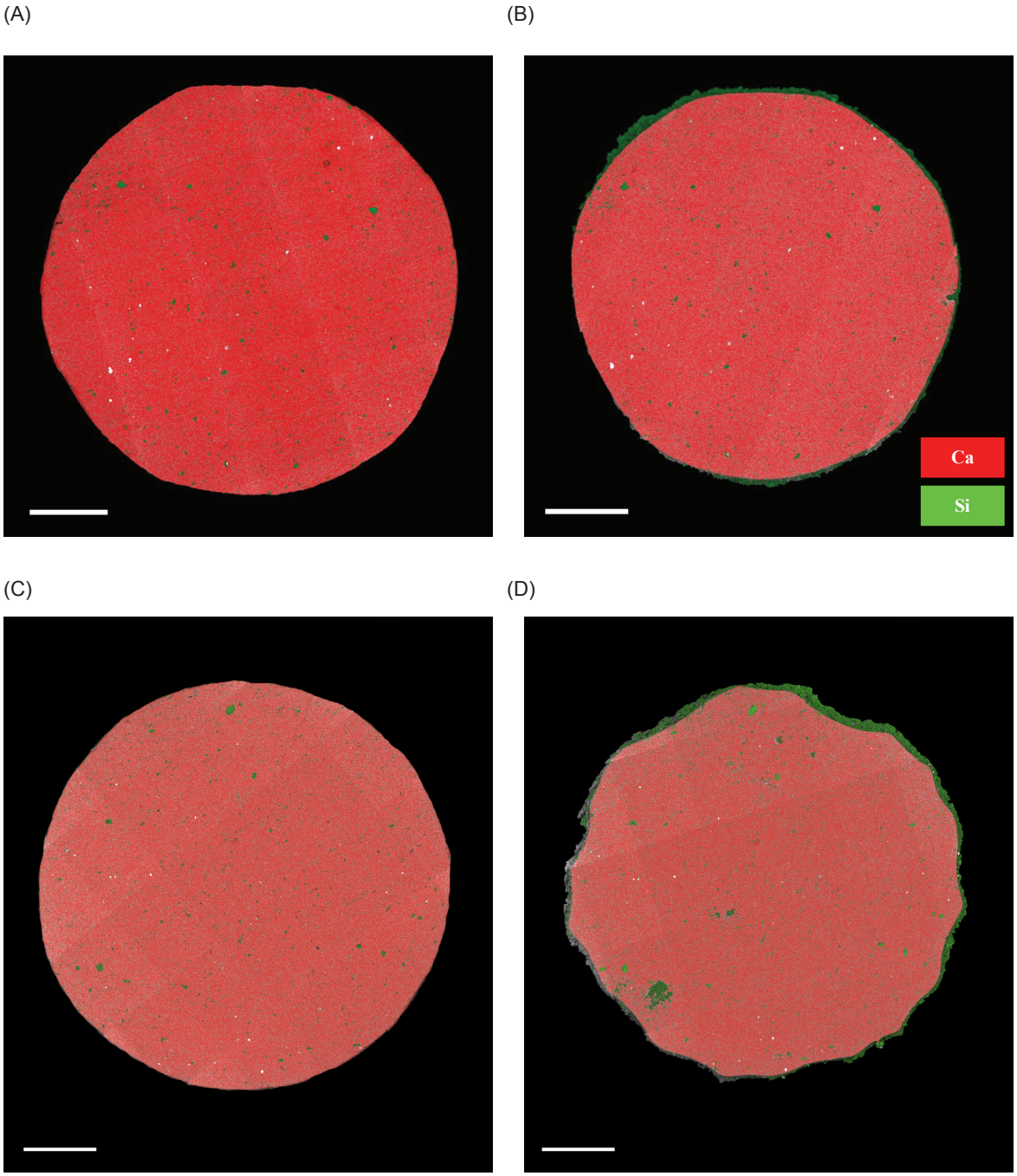


Fig. 5 (A) MCR5 rock sample before single-phase reaction (B) MCR5 rock sample after single-phase reaction (C) MCR6 rock sample before multiphase reaction (D) MCR6 rock sample after multiphase reaction. Scale bar is $500\mu m$

acid concentration increases beyond a point where gas phase no longer dissolves into surrounding HCl solution and starts to nucleate at the reactive surface (Figure 3C). We find that there can be one order of magnitude of deviation between the rate law and the measured effective reaction rate, though there is good agreement between the single phase dissolution rate and the early stage of multiphase dissolution. The bubbles continue to grow and coalesce into larger bubbles to a point where they surround most of

View Article Online
DOI: 10.1039/D5LC00557D

Published on 15 August 2025. Downloaded by Yunnan University on 8/23/2025 5:33:34 PM.

the reactive surface, significantly shielding the available surface for reaction and reducing the effective reaction rate drastically below its estimated rate. Our results indicate the state-of-the-art model for multiphase reactive dissolution will largely underestimate the shielding effect of bubbles if the gas phase is generated from the reactive interface. In this study, we demonstrated that ML-enabled image segmentation combined with physics-based modeling is a powerful tool to quantify the dynamics of geochemical reactions and extend the potential of sample-embedded microfluidic devices. Such methodology allows continuous monitoring and calculation of dynamic properties, such as reaction rate, without saturating reaction chambers with an inert fluorescent solution that only allows quantification of reacted mineral area before and after reaction as previously shown[35]. We also find that the chemical heterogeneity of the rock results in the formation of an unreacted porous layer surrounding the rock sample, which serves as a support for CO_2 bubbles nucleation and physically separates them from the moving reactive interface. This new finding changes the conceptualization for multiphase dissolution reactions in naturally heterogenous rocks, and lays the foundation for the development of quantitative models correlating effective reaction rates to mineral composition. Current work involves quantifying the impact of secondary minerals on the transport properties of the unreacted porous layer as well as on the overall rock effective reactivity for different carbonate contents and spatial distribution of the mineral species.

Author contributions

J.H., S.Y. and I.B. designed the research; J.H. and S.Y. performed the research; C.M.R. contributed new analytic tools; J.H., S.Y., C.M.R., and I.B. analyzed data; J.H. and S.Y. wrote the paper first draft; J.H., S.Y., C.M.R., and I.B. wrote the final draft.

Conflicts of interest

There are no conflicts to declare.

Data availability

The data supporting this article have been included as part of the Supplementary Information.

Acknowledgements

This work was supported as part of the Center for Mechanistic Control of Unconventional Formations, an Energy Frontier Research Center funded by US Department of Energy, Office of Science, Basic Energy Sciences Award DE-SC0019165. All micromodels used in this study were fabricated at Stanford Nanofabrication Facility (SNF), part of the Stanford Nano Shared Facilities (SNSF) supported by the National Science Foundation under award ECCS-2026822. SEM-based imaging was performed in the shared analytical facilities of Stanford Doerr School of Substainability.

Notes and references

1 B. I. McNeil and R. J. Matear, *Proceedings of the National Academy of Sciences*, 2008, **105**, 18860–18864.

2 O. Sulpis, B. P. Boudreau, A. Mucci, C. Jenkins, D. S. Trossman, B. K. Arbic and R. M. Key, *Proceedings of the National Academy of Sciences*, 2018, **115**, 11700–11705.

3 E. C. Geyman, Z. Wu, M. D. Nadeau, S. Edmonsond, A. Turner, S. J. Purkis, B. Howes, B. Dyer, A.-S. C. Ahm, N. Yao *et al.*, *Proceedings of the National Academy of Sciences*, 2022, **119**, e2210617119.

4 A. V. Subhas, J. F. Adkins, N. E. Rollins, J. Naviaux, J. Erez and W. M. Berelson, *Proceedings of the National Academy of Sciences*, 2017, **114**, 8175–8180.

5 K. J. Sathaye, M. A. Hesse, M. Cassidy and D. F. Stockli, *Proceedings of the National Academy of Sciences*, 2014, **111**, 15332–15337.

6 K. Z. House, D. P. Schrag, C. F. Harvey and K. S. Lackner, *Proceedings of the National Academy of Sciences*, 2006, **103**, 12291–12295.

7 A. Al-Yaseri, H. Al-Mukainah, N. Yekeen and A. S. Al-Qasim, *International Journal of Hydrogen Energy*, 2023, **48**, 3583–3592.

8 J. P. Fitts and C. A. Peters, *Reviews in Mineralogy and Geochemistry*, 2013, **77**, 459–479.

9 F. G. Bell, *Environmental geology*, 1993, **21**, 187–200.

10 J. W. Morse and R. S. Arvidson, *Earth-Science Reviews*, 2002, **58**, 51–84.

11 A. L. Harrison, A. D. Jew, M. K. Dustin, D. L. Thomas, C. M. Joe-Wong, J. R. Bargar, N. Johnson, G. E. Brown Jr and K. Maher, *Applied Geochemistry*, 2017, **82**, 47–62.

12 C. Luo, J. Routh, M. Dario, S. Sarkar, L. Wei, D. Luo and Y. Liu, *Science of the Total Environment*, 2020, **724**, 138122.

13 W. Song, F. Ogunbanwo, M. Steinsbø, M. A. Fernø and A. R. Kovscek, *Lab on a Chip*, 2018, **18**, 3881–3891.

14 D. Picchi and I. Battiato, *Water Resources Research*, 2018, **54**, 6683–6707.

15 P. Li, H. Deng and S. Molins, *Frontiers in Water*, 2022, **3**, 734518.

16 J. Jiménez-Martínez, T. Le Borgne, H. Tabuteau and Y. Méheust, *Water Resources Research*, 2017, **53**, 1457–1472.

17 J. Jiménez-Martínez, J. D. Hyman, Y. Chen, J. W. Carey, M. L. Porter, Q. Kang, G. Guthrie Jr. and H. S. Viswanathan, *Geophysical Research Letters*, 2020, **47**, e2020GL087163.

18 H. Liu, C. Doughty and G. Bodvarsson, *Water Resources Research*, 1998, **34**, 2633–2646.

19 T. Xu, E. Sonnenthal, N. Spycher and K. Pruess, *TOUGHREACT user's guide: A simulation program for non-isothermal multiphase reactive geochemical transport in variable saturated geologic media*, Lawrence berkeley national lab.(lbnl), berkeley, ca (united states) technical report, 2004.

20 J. Maes and H. P. Menke, *Transport in Porous Media*, 2021, **139**, 271–299.

21 Y. Al-Khulaifi, Q. Lin, M. J. Blunt and B. Bijeljic, *Water Resources Research*, 2019, **55**, 3171–3193.

22 D. Prokhorov, V. Lisitsa, T. Khachkova, Y. Bazaikin and Y. Yang, *Journal of Computational Science*, 2022, **58**, 101550.

23 C. Noiriel and C. Soulaine, *Transport in Porous Media*, 2021, **140**, 181–213.

Lab on a Chip Accepted Manuscript

View Article Online
DOI: 10.1039/D5LC00557D

Published on 15 August 2025. Downloaded by Yunnan University on 8/23/2025 5:33:34 PM.

24 A.-M. Eckel, R. Liyanage, T. Kurotori and R. Pini, *Industrial & Engineering Chemistry Research*, 2022.

25 H. P. Menke, B. Bijeljic, M. G. Andrew and M. J. Blunt, *Environmental science & technology*, 2015, **49**, 4407–4414.

26 S. S. Datta, I. Battiato, M. A. Fernø, R. Juanes, S. Parsa, V. Prigiobbe, E. Santanach-Carreras, W. Song, S. L. Biswal and D. Sinton, *Lab on a Chip*, 2023, **23**, 1358–1375.

27 W. Song, T. W. de Haas, H. Fadaei and D. Sinton, *Lab on a Chip*, 2014, **14**, 4382–4390.

28 W. Song and A. R. Kovscek, *Journal of Natural Gas Science and Engineering*, 2016, **34**, 1276–1283.

29 W. Yun, C. M. Ross, S. Roman and A. R. Kovscek, *Lab on a Chip*, 2017, **17**, 1462–1474.

30 C. Soulaine, S. Roman, A. R. Kovscek and H. A. Tchelepi, *Journal of Fluid Mechanics*, 2017, **827**, 457–483.

31 C. T. Gerold, A. T. Krummel and C. S. Henry, *Microfluidics and Nanofluidics*, 2018, **22**, 76.

32 C. Soulaine, S. Roman, A. Kovscek and H. A. Tchelepi, *Journal of Fluid Mechanics*, 2018, **855**, 616–645.

33 H. Fazeli, M. Nooraiepour and H. Hellevang, *Industrial and Engineering Chemistry Research*, 2020, **59**, 450–457.

34 B. Ling, H. J. Khan, J. L. Druhan and I. Battiato, *Energies*, 2020, **14**, 21.

35 B. Ling, M. Sodwatana, A. Kohli, C. M. Ross, A. Jew, A. R. Kovscek and I. Battiato, *Proceedings of the National Academy of Sciences*, 2022, **119**, 1–9.

36 J. Poonoosamy, A. Kaspor, C. Schreinemachers, D. Bosbach, O. Cheong, P. M. Kowalski and A. Obaied, *Scientific Reports*, 2024, **14**, 9502.

37 M. I. Lönartz, Y. Yang, G. Deissmann, D. Bosbach and J. Poonoosamy, *Water resources research*, 2023, **59**, e2023WR034722.

38 F. Weinhardt, J. Deng, J. Hommel, S. Vahid Dastjerdi, R. Gerlach, H. Steeb and H. Class, *Transport in Porous Media*, 2022, **143**, 527–549.

39 J. Poonoosamy, C. Soulaine, A. Burmeister, G. Deissmann, D. Bosbach and S. Roman, *Lab on a Chip*, 2020, **20**, 2562–2571.

40 W. Song, T. W. de Haas, H. Fadaei and D. Sinton, *Lab Chip*, 2014, **14**, 4382–4390.

41 W. Song and A. R. Kovscek, *Lab on a Chip*, 2015, **15**, 3314–3325.

42 C.-X. Zhou, R. Hu, H. Deng, B. Ling, Z. Yang and Y.-F. Chen, *Geophysical Research Letters*, 2023, **50**, e2023GL104067.

43 S. Berg, D. Kutra, T. Kroeger, C. N. Straehle, B. X. Kausler, C. Haubold, M. Schiegg, J. Ales, T. Beier, M. Rudy *et al.*, *Nature methods*, 2019, **16**, 1226–1232.

44 H.-J. Cho and J. Choi, *Journal of Marine Science and Engineering*, 2019, **7**, 457.

45 K. Lund, H. S. Fogler, C. McCune and J. Ault, *Chemical Engineering Science*, 1975, **30**, 825–835.

46 F. Gray, B. Anabaraonye, S. Shah, E. Boek and J. Crawshaw, *Advances in water resources*, 2018, **121**, 369–387.

47 C. Soulaine, S. Roman, A. Kovscek and H. A. Tchelepi, *Journal of Fluid Mechanics*, 2017, **827**, 457–483.

48 W. Song, H. Fadaei and D. Sinton, *Environmental science & technology*, 2014, **48**, 3567–3574.

49 G. Dávila, L. Luquot, J. M. Soler and J. Cama, *International Journal of Greenhouse Gas Control*, 2016, **48**, 105–119.

50 H.-H. Liu, G. Zhang and G. S. Bodvarsson, *Vadose Zone Journal*, 2003, **2**, 259–269.

Lab on a Chip Accepted Manuscript

View Article Online
DOI: 10.1039/D5LC00557D

Data availability statement

The data supporting this article have been included as part of the Supplementary Information.

Published on 15 August 2025. Downloaded by Yunnan University on 8/23/2025 5:33:34 PM.

Lab on a Chip Accepted Manuscript